aerospace

MDPI

Article

Application of a Soft-Switching Adaptive Kalman Filter for Over-Range Measurements in a Low-Frequency Extension of MHD Sensors

Junze Tong [1,2], Shaocen Shi [1,2], Fuchao Wang [1] and Dapeng Tian [1,2,*]

1 Changchun Institute of Optics, Fine Mechanics and Physics, Chinese Academy of Sciences, Changchun 130033, China; tongjunze20@mails.ucas.ac.cn (J.T.); shishaocen23@mails.ucas.ac.cn (S.S.); wangfuchao@ciomp.ac.cn (F.W.)

2 University of the Chinese Academy of Sciences, Beijing 100049, China

* Correspondence: d.tian@ciomp.ac.cn

Abstract: The increasing demand for image quality in aerospace remote sensing has led to higher performance requirements for inertial stabilization platforms equipped with image sensors, particularly in terms of bandwidth. To achieve wide-bandwidth control in optical stabilization platforms, engineers employ magneto-hydrodynamic (MHD) sensors as key components to enhance system performance because of their wide measurement bandwidth (5–1000 Hz). While MHD sensors offer a wide-frequency response, they are limited by a narrow measuring range and low sensitivity at low frequencies, making them unsuitable as standalone sensors. To address the challenges of over-range measurement and the loss of low-frequency signals, in this study, we developed a soft-switching adaptive Kalman filter method, which enables us to dynamically adjust the fusion weights in the Kalman filter so we can obtain wide-band measurement signals even when the MHD sensor experiences over-range conditions. The proposed method was validated with fusion experiments involving a fiber-optic gyroscope and an MHD sensor; the results demonstrate its ability to expand the sensing bandwidth, regardless of the operating conditions of the MHD sensor.

Keywords: MHD; adaptive law; Kalman filter; inertial sensors; data fusion

check for updates

Academic Editors: Hang Guo and Yan (Rockee) Zhang

Received: 18 December 2024
Revised: 18 February 2025
Accepted: 26 February 2025
Published: 27 February 2025

Citation: Tong, J.; Shi, S.; Wang, F.; Tian, D. Application of a Soft-Switching Adaptive Kalman Filter for Over-Range Measurements in a Low-Frequency Extension of MHD Sensors. *Aerospace* **2025**, *12*, 192. https://doi.org/10.3390/aerospace12030192

1. Introduction

Aerial remote sensing imaging technology has numerous applications in modern fields, such as environmental monitoring, disaster management, agricultural analysis, and urban planning [1–3]. However, the complex aviation environment introduces multi-source interference, significantly affecting the stability and tracking accuracy of aerial remote sensing systems [4,5]. To achieve high-resolution, high-precision imagery, engineers employ aerial remote sensing stabilization platforms to connect photoelectric sensors to the carrier so that the aiming line of the sensor remains stable relative to the imaging area in inertial space [6]. As the key components of the inertial stabilization platform, inertial sensors provide essential feedback signals that help stabilize the optical sensor's aiming line by detecting attitude changes in the stabilization platform [7].

Traditional inertial angular velocity sensors operate on various principles, but they all have inherent limitations as shown in Table 1 [8]. Magneto-hydrodynamic (MHD) inertial sensors represent a valuable supplement to traditional inertial measurement technologies [9]. Based on MHD principles, MHD sensors detect acceleration and angular velocity without mechanical wear, and they offer a wide-frequency response and high impact resistance [10]. Nevertheless, because of limitations in inertial sensor hardware and technology, existing standalone angular velocity sensors struggle to measure small angular vibrations and cover the full frequency range simultaneously [11,12]. As a result, these sensors are often insensitive to high-frequency external disturbances, limiting the control system's ability to suppress high-frequency interference [13]. To address this, expanding the measurement bandwidth is crucial without compromising imaging stability. Combining sensors with different frequency band characteristics through data fusion has proven to be an effective solution [14–17].

Table 1. Limitation and measurement frequency band of traditional sensors.

Type	Limitations	Common Frequency Band
MEMS Gyroscope	Low accuracy and Weak anti-interference.	0∼200 Hz
Fiber optic Gyroscope	Low frequency drift exists.	0∼400 Hz
Accelerator	Measuring linear acceleration only.	0∼5 kHz
MHD sensors	Low frequency cannot be measured.	2∼1 kHz

Note: The term "common frequency band" refers to products that are widely used and does not include specially made items. The content above encompasses applications across various fields. In the field of aerial imaging, the cut-off frequency of commonly used IMUs (which integrate gyroscopes and accelerometers) typically ranges from 100 to 200 Hz.

In aerospace optical imaging or inertial navigation fields, stable platforms commonly use inertial angular velocity sensors such as Micro-Electro-Mechanical Systems (MEMS) gyroscopes and Fiber-Optic Gyroscopes (FOGs) [18,19]. However, due to the nature of gyroscopes, the integration angular measurement tends to drift. To address this drift, engineers typically use the Extended Kalman Filter or other method to combine gyroscopes with accelerators or magnetometers to achieve a multi-axis Inertial Measurement Unit (IMU) [20–22]. For this fusion, the measurement bandwidth is usually not considered, but bandwidth matching is necessary, meaning that multiple sensors should have similar bandwidths. Especially long-focus photography is highly sensitive to vibration, it is essential to suppress the high-frequency vibration of the optical stabilization platform. In response to this issue, this paper focuses on the expansion of the bandwidth of MHD sensors and explores a sensor fusion scheme to extend their low-frequency measurement capabilities.

Sensor fusion algorithms can be broadly categorized into time- and frequency–domain methods [23]. Complementary and closed-loop control filtering are classical frequency–domain data fusion approaches. Complementary filtering is simple. It does not involve complex matrix operations, but it heavily depends on the accurate modeling of the transfer function of the sensors being fused, and its weights cannot be adapted dynamically to environmental noise or motion states [24]. Closed-loop control filtering, which fuses controller outputs, feedback signals, and setpoints, effectively reduces noise influence and prevents overshoots or oscillations caused by sudden changes [25]. However, traditional closed-loop control filters lack a clear design method, making parametric design challenging.

In contrast, Wiener filters [26], Kalman filters [27], and similar algorithms are time domain-based fusion methods that allow for the optimal estimation of signals containing noise. Kalman filtering is a classical signal fusion technique suitable for linear systems [28]. It features simple iterative operations and uses residual state predictions for signal correction, effectively filtering out both white noise and colored noise. Many filtering algorithms, such as the extended Kalman filter [29] and the unscented Kalman filter [30], have been developed based on the basic Kalman filter. The Kalman gain determines the balance between the predicted states and the actual measurements, and process noise covariance **Q** and measurement noise covariance **R** directly influence the size of this gain. The proper selection and adaptive adjustment of **Q** and **R** are key to ensuring stable Kalman filter performance in complex environments, thereby providing accurate estimations [31,32].

Regarding the optimization and parameter tuning of the Kalman filtering method, researchers have proposed various adaptive Kalman filtering approaches. Adaptive Kalman filters can be used to dynamically adjust the filtering parameters according to real-time signal characteristics, adapting to varying noise levels under different working conditions to enhance system stability [33]. The recursive least squares method is often used to calculate the variance of system residuals, with improvements such as removing the rounding operations of the original algorithm to increase sensitivity to errors [34]. Additionally, a noise covariance adaptive update mechanism based on covariance matching can be used to correct process noise covariance **Q** and measurement noise covariance **R** in real time [35]. By adjusting **Q** and **R** based on residuals derived from application scenario feedback, we can update the noise covariance matrix dynamically, ensuring the filter provides optimal state estimation under the current dynamic conditions [36]. The adaptive Kalman filtering approach based on model parameter ratios further enhances filter robustness in uncertain environments, though it requires the balancing of noise estimation accuracy with computational complexity [37,38].

Given that FOGs offer higher precision than MEMS gyroscopes and exhibit low-pass characteristics in the frequency domain, this study implements the fusion of MHD sensors with a FOG using a Kalman filter scheme. However, the measurement range of MHD sensors is constrained by the secondary amplification coil and operational amplifier circuit, resulting in a trade-off between measurement range and sensitivity. During the sensor fusion process with the Kalman filter, saturation caused by the limited measurement range can introduce errors in the fusion results. To address this issue, we propose an adaptive Kalman filtering method with a soft-switching function. With this method, one can detect the saturation state of the measurements with an adaptive function, using a soft-switching adaptive function to adjust the **R** matrix, altering the weight of the measurements in the fusion process, and ensuring the accuracy of the fusion results under different operating conditions.

The structure of this paper is as follows: In Section 2, we describe the measurement principle of the MHD sensor and discuss the associated issues. In Section 3, we present the proposed SSAKF fusion scheme designed to address previous issues. In Section 4, we provide the simulation results. In Section 5, we report on the validation of the superiority of the proposed method based on comparisons with two other fusion methods in four different experiments. In Section 6, we present our conclusions.

2. MHD Sensor Principle and Limitations

This section explains the measurement principle of MHD sensors, along with the transfer function for MHD measurement and the significance of its corresponding parameters. The limitations arising from this measurement principle and the issues that need to be addressed are also discussed.

2.1. Measuring Principle of MHD

Figure 1 delineates the operational mechanism of an MHD sensor. The fundamental constituents of this sensing arrangement consist of an annular vessel containing an electrically conductive fluid, a permanent magnet, and a set of electrodes positioned on both the inner and outer walls of the annular vessel. When the support structure on which the sensor is mounted rotates at an angular velocity ω, the conductive fluid remains relatively static in relation to the inertial frame of reference because of inertia and the fluid's viscous properties. This results in a relative velocity v between the fluid and the rotating magnetic field. Consequently, as the conducting fluid traverses the magnetic field, it produces an induced electromotive force (EMF) E at the electrodes. By measuring E, the angular velocity ω of the inertia can be derived [39,40].

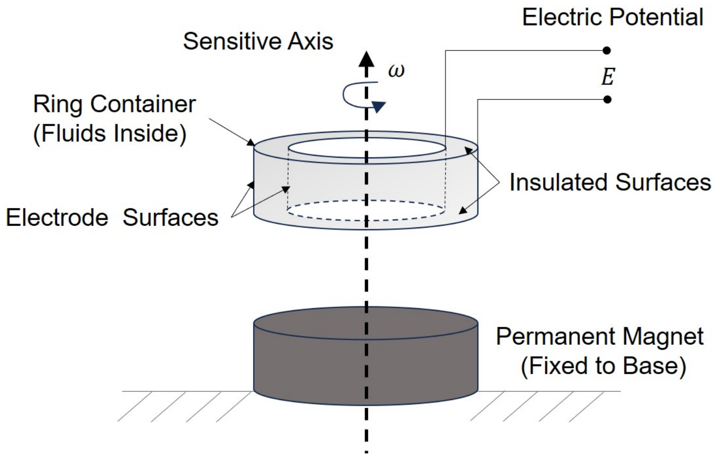

Figure 1. The mechanism of an MHD sensor.

2.2. Limitations in Measurement with MHD Sensors

MHD sensors cannot measure low-frequency signals because, at lower motion frequencies, the viscous forces within the conductive fluid prevent them from staying completely stationary relative to the inertial system. As a result, the fluid becomes synchronized with the motion of the surrounding container, causing a decrease in relative velocity and the induced EMF E. Based on the dynamic properties of the fluid and its operational principles, the transfer function of the induced EMF can be expressed as [41]

$$\frac{E(s)}{\omega(s)} = \frac{BWrs}{s + \frac{\nu(1+H^2)}{h^2}}, \tag{1}$$

where the parameters in Equation (1) are defined in Table 2, and s means a complex variable in the Laplace transform.

Table 2. Parameter definitions for the MHD measurement equation.

Parameter	Definition	Unit
B	Magnetic induction generated by permanent magnets	T
W	Width of ring container, $W = r_o - r_i$, r_o and r_i represents the inner and outer radius.	m
r	Radius Root Mean Square of ring container, $r = \sqrt{r_o^2 + r_i^2}$	m
ν	Viscosity coefficient of conductive fluids	m^2/s
h	Height of ring container	m
H	Hartmann's constant, $H = Bh/\sqrt{\rho\nu\eta}$	
ρ	Density of conductive fluids	kg/m^3
η	Resistivity of conductive fluids	$\Omega{\cdot}m$

The cutoff frequency ω_c of the MHD sensor is given by

$$\omega_c = \frac{\nu(1+H^2)}{h^2} = \frac{\nu}{h^2} + \frac{B^2}{\rho\eta}. \tag{2}$$

By analyzing Equation (2), we see that the only way to reduce the cutoff frequency without modifying the magneto-fluidic material is to either increase the height h of the ring container or decrease the magnetic field strength B of the permanent magnet. However, the design parameters of MHD systems are constrained by strict size and sensitivity requirements in aerospace applications, making adjustments to the MHD design challenging. As a result, expanding the low-frequency bandwidth of MHD sensors is difficult. This limitation is why MHD sensors cannot be used standalone and must be integrated with other sensors to extend their low-frequency measurement range.

In addition, the MHD sensor's backend requires the design of a secondary amplification circuit. To balance measurement accuracy and amplification range, the MHD sensor's measurement range is limited to ±0.5 rad/s. When the sensor's measurement range exceeds its capacity, the measurement results become distorted, making it impossible to reflect the true data. Therefore, this issue must be carefully considered in the fusion measurement scheme.

As a complementary solution in both temporal and frequency domains, FOG serve as an optimal choice. Based on the Sagnac effect, FOG perform interference measurements to detect the angular velocity of rigidly connected platforms. In the frequency domain, they exhibit low-pass characteristics, with typical commercial products offering bandwidths of 100–400 Hz, while high-performance variants can reach nearly kHz levels. Beyond frequency–domain advantages, FOG demonstrate a temporal measurement range of 400°/s to 1000°/s, effectively avoiding over-range issues in aviation imaging stabilization platforms. These attributes make FOG the selected low-frequency extension scheme for MHD sensors in this study.

3. SSAKF Design

Kalman filters are widely used in sensor fusion problems. In this section, we present a low-frequency expansion scheme for MHD sensors based on the traditional Kalman filter. We also demonstrate, based on the conducted simulations, the issues that arise when the MHD sensor exceeds its range. To address the problem of over-range measurement, we propose an improved adaptive Kalman filtering equation and provide corresponding simulation cases.

3.1. Traditional Kalman Filter Design

We define a discrete linear system

$$\begin{cases} \mathbf{x}(k) = \mathbf{A}\mathbf{x}(k) + \mathbf{B}\mathbf{u}(k) + \mathbf{w}(k) \\ \mathbf{z}(k) = \mathbf{H}\mathbf{x}(k) + \mathbf{v}(k), \end{cases} \tag{3}$$

where k is the moment of sampling, $\mathbf{x}(k)$ is the state of the system, $\mathbf{z}(k)$ is the measurement, $\mathbf{A}$ is the state transfer matrix, $\mathbf{B}$ is the input matrix, $\mathbf{u}(k)$ is the input quantity, $\mathbf{H}$ is the measurement matrix, $\mathbf{w}(k)$ is random noise in the system, and $\mathbf{v}(k)$ is the measurement noise.

The traditional Kalman filter consists of five classical equations, which can be divided into two parts: a priori prediction, given by

$$\begin{cases} \hat{\mathbf{x}}^-(k) = \mathbf{A}\hat{\mathbf{x}}^-(k-1) + \mathbf{B}\mathbf{u}(k) \\ \mathbf{P}^-(k) = \mathbf{A}\mathbf{P}(k-1)\mathbf{A}^T + \mathbf{Q}, \end{cases} \tag{4}$$

and a posteriori correction, given by

$$\begin{cases} \mathbf{K}(k) = \mathbf{P}^-(k)\mathbf{H}^T(\mathbf{H}\mathbf{P}^-(k)\mathbf{H}^T + \mathbf{R})^{-1} \\ \hat{\mathbf{x}}(k) = \hat{\mathbf{x}}^-(k) + \mathbf{K}(k)[\mathbf{z}(k) - \mathbf{H}\hat{\mathbf{x}}^-(k)] \\ \mathbf{P}(k) = (\mathbf{I} - \mathbf{K}(k)\mathbf{H})\mathbf{P}^-(k). \end{cases} \tag{5}$$

In these equations, $(\cdot)^{-}$ denotes prior data, and $\mathbf{Q}$ and $\mathbf{R}$ represent the covariance matrices of system noise and measurement noise, respectively, $\mathbf{P}$ means the posteriori estimate covariance matrix, and $\mathbf{I}$ is a unit matrix of suitable dimension.

For the low-frequency extension of the MHD, an FOG with low-pass characteristics is used for data fusion. The transfer functions of the two sensors are

$$\begin{cases} G_{FOG}(s) = \frac{\omega_{FOG}}{s+\omega_{FOG}} \\ G_{MHD}(s) = \frac{s}{s+\omega_{MHD}}, \end{cases} \tag{6}$$

where ω_{FOG} and ω_{MHD} are the cutoff angular frequencies for the FOG and MHD, respectively. Then, the equation of state in its continuous domain is obtained as

$$\begin{bmatrix} \dot{x}_1(t) \\ \dot{x}_2(t) \end{bmatrix} = \begin{bmatrix} -\omega_{FOG} & 0 \\ 0 & -\omega_{MHD} \end{bmatrix} \begin{bmatrix} x_1(t) \\ x_2(t) \end{bmatrix} + \begin{bmatrix} 1 \\ 1 \end{bmatrix} \omega(t) \tag{7}$$

$$\begin{bmatrix} z_1(t) \\ z_2(t) \end{bmatrix} = \begin{bmatrix} \omega_{FOG} & 0 \\ 0 & -\omega_{MHD} \end{bmatrix} \begin{bmatrix} x_1(t) \\ x_2(t) \end{bmatrix} + \begin{bmatrix} 0 \\ 1 \end{bmatrix} \omega(t), \tag{8}$$

where $z_1(t)$ is the FOG measurement value, and $z_2(t)$ is the MHD measurement value.

Now, we also expand the angular velocity as a state variable in $\mathbf{x}(k)$, then discrete it according to the backward Euler method with a sampling time of t_s:

$$\begin{bmatrix} \omega(k) \\ x_1(k) \\ x_2(k) \end{bmatrix} = \begin{bmatrix} 1 & 0 & 0 \\ t_s/(\omega_{FOG}t_s+1) & 1/(\omega_{FOG}t_s+1) & 0 \\ t_s/(\omega_{MHD}t_s+1) & 0 & 1/(\omega_{MHD}t_s+1) \end{bmatrix} \begin{bmatrix} \omega(k-1) \\ x_1(k-1) \\ x_2(k-1) \end{bmatrix} \tag{9}$$

$$\begin{bmatrix} z_1(k) \\ z_2(k) \end{bmatrix} = \begin{bmatrix} 0 & \omega_{FOG} & 0 \\ 1 & 0 & -\omega_{MHD} \end{bmatrix} \begin{bmatrix} \omega(k) \\ x_1(k) \\ x_2(k) \end{bmatrix}. \tag{10}$$

We see that matrix $\mathbf{H}$ in the measurement in Equation (10) is not square. Therefore, when solving for the Kalman gain, we need to ensure that the singularity problem does not arise by computing the generalized inverse of the matrix. Since matrix $\mathbf{H}$ has full column rank, the Kalman gain ($\mathbf{K}(k)$) can be recalculated as

$$\mathbf{K}(k) = \mathbf{P}^{-}(k)\mathbf{H}^T\mathbf{S}(k)^{-1} = \mathbf{P}^{-}(k)\mathbf{H}^T\mathbf{S}(k)^T[\mathbf{S}(k)\mathbf{S}(k)^T]^{-1}, \tag{11}$$

where $\mathbf{S}(k) = \mathbf{H}\mathbf{P}^{-}(k)\mathbf{H}^T + \mathbf{R}$.

However, when the MHD sensor is under an over-range measurement condition, the measured value does not conform to the dynamic characteristics of the sensor. Therefore, a new solution must be proposed for this condition to avoid fusion errors caused by over-range measurement issues.

3.2. Soft-Switching Adaptive Method

We analyze the estimation results ($\hat{\mathbf{x}}(k)$) to the Kalman filter equation from another perspective. Based on the matrix inversion lemma $(\mathbf{A}+\mathbf{BCD})^{-1} = \mathbf{A}^{-1} - \mathbf{A}^{-1}\mathbf{B}(\mathbf{D}\mathbf{A}^{-1}\mathbf{B} + \mathbf{C}^{-1})^{-1}\mathbf{D}\mathbf{A}^{-1}$, Equation (5) can be rewritten as

$$\begin{cases} \mathbf{P}(k) = [(\mathbf{P}^{-}(k))^{-1} + \mathbf{H}^T\mathbf{R}^{-1}\mathbf{H}]^{-1} \\ \hat{\mathbf{x}}(k) = \mathbf{C}_p(k)\hat{\mathbf{x}}^{-}(k) + \mathbf{C}_m(k)\mathbf{z}(k), \end{cases} \tag{12}$$

where the predictive coefficient is given by $\mathbf{C}_p(k) = \mathbf{P}(k)(\mathbf{P}^{-}(k))^{-1}$, and the measurement coefficient is $\mathbf{C}_m(k) = \mathbf{P}(k)\mathbf{H}^T\mathbf{R}^{-1}$. A detailed derivation process can be found in Appendix A. State $\hat{\mathbf{x}}(k)$ can be expressed as a linear combination of a priori state $\hat{\mathbf{x}}^{-}(k)$ and measurement (k). From the expression of the linear combination, the elements in matrix $\mathbf{R}$ directly affect the weight of measurement $\mathbf{z}(k)$ in the estimation result. Based on this, by increasing the values in matrix $\mathbf{R}$, the influence of $\mathbf{z}(k)$ can be reduced, thereby suppressing the effect of the MHD measurement on the fusion result.

Based on this idea, a soft-switching adaptive method, with which one can adjust the corresponding parameters in matrix $\mathbf{R}$ based on whether the measurement value exceeds the range, is proposed:

$$\begin{cases} \bar{\mathbf{R}}(k) = \mathbf{D}_{ck}\mathbf{\Omega}(k)\mathbf{D}_{ck}^{T} \\ \mathbf{R} = \mathbf{D}_{ck}\mathbf{D}_{ck}^{T} \\ \mathbf{\Omega}(k) = diag[f(z_1(k)), \cdots, f(z_n(k))] \\ f(z) = (\tanh(\alpha(|z| - \tau)) + 1)\beta + 1. \end{cases} \tag{13}$$

In the adaptive function in Equation (13), employing the Cholesky decomposition ensures that transformed matrix $\bar{\mathbf{R}}(k)$ retains its symmetry; thus, $\mathbf{D}_{ck}$ is the Cholesky decomposition of matrix $\mathbf{R}$. The function $f(\cdot)$ is the adaptive function, where τ denotes the threshold, α represents the rate at which the function increases above the threshold, β affects the function maximum, and z_i denotes the ith measurement. The function plot is shown in Figure 2.

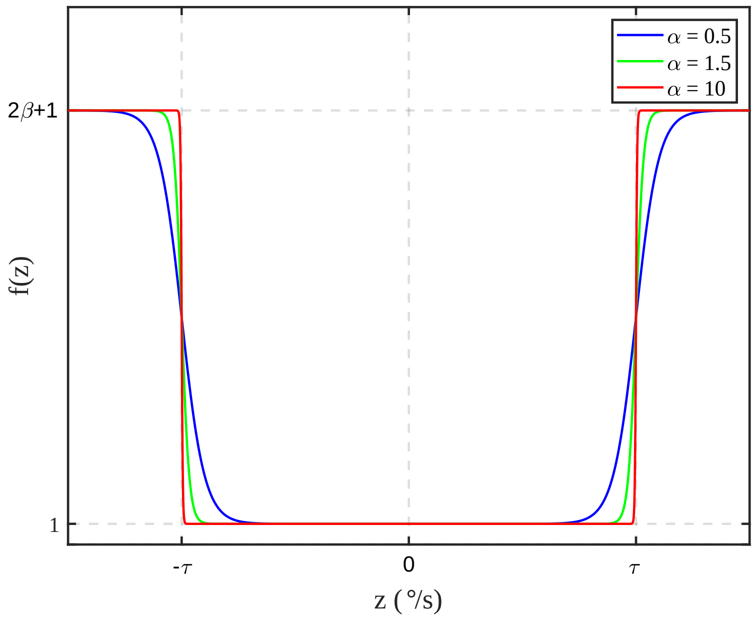

Figure 2. Adaptive function $f(z)$.

Notably, when the variable is less than τ, the function value approaches 1. However, as the variable approaches τ, the function value increases, reaching a maximum value of $2\beta + 1$, with the rate of increase depending on α. Using this method, we can adaptively adjust matrix $\bar{\mathbf{R}}(k)$ based on whether the measured value is out of range. At the same time, the symmetry of matrix $\bar{\mathbf{R}}(k)$ is ensured, and this matrix replaces matrix $\mathbf{R}$ in Equation (5).

Additionally, it should be noted that, when the SSAKF method fuses measurements, all measured values cannot be potentially become saturated, at least one of the signals always needs to be used as the fusion reference. This conclusion is self-evident: when neither of all values is accurate, the fused result cannot be reliable.

Above all, the soft-switching of the parameters in matrix $\bar{\mathbf{R}}(k)$ is achieved with the asymptotic form of the $tanh(\cdot)$ function, which avoids the undesirable abrupt dynamic behavior in the estimation results caused by direct parameter changes.

4. SSAKF Simulations

This section reports the simulated fusion results of the traditional Kalman filter and the SSAKF under different conditions. The effectiveness of the proposed method is verified through simulations.

4.1. Traditional Kalman Filter Simulation

This simulation focused on the effectiveness of the conventional Kalman filter when the MHD sensor measures whether the signal exceeds the range. The practical nominal transfer function of the sensor was used in the simulation (the detailed model identification is displayed in Section 5.1). The cutoff frequency of the FOG measurement was approximately 100 Hz ($\omega_{FOG} \approx 200\pi$), while that of the MHD measurement was approximately 5.3 Hz ($\omega_{MHD} \approx 10.6\pi$). The measurement range of the MHD was consistent with the actual range of ±0.5 rad/s, and the sampling time was 0.5 ms.

The actual velocity signal ($\omega(t)$) was obtained from a series of the sine signals ($u(t)$) passing through a motor model $G_{motor}(s) = 1/(0.0005s + 0.0125)$. The $u(t)$ signal also includes white noise $n(t)$, which follows a Gaussian distribution:

$$u(t) = A \cdot [\sin(2\pi \cdot 0.2t) + \sin(2\pi \cdot 4.5t) + \sin(2\pi \cdot 20t)\sin(2\pi \cdot 400t)] + n(t). \tag{14}$$

According to Equation (14), $u(t)$ includes different frequency components. The amplitude A was used to adjust the signal magnitude to produce the saturation of the measurement. We assumed that noise $n(t) \sim N(0, 0.01)$. The measurement noise (n_{FOG}) was assumed to satisfy $n_{FOG} \sim N(0, 0.01)$, and n_{MHD} was assumed to satisfy $n_{MHD} \sim N(0, 0.05)$.

According to the above input condition, the matrix in Equation (3) can be calculated as

$$\mathbf{A} = \begin{bmatrix} 1 & 0 & 0 \\ 0.0004 & 0.7609 & 0 \\ 0.0005 & 0 & 0.9836 \end{bmatrix} \quad \mathbf{H} = \begin{bmatrix} 0 & 628.3185 & 0 \\ 1 & 0 & -33.3009 \end{bmatrix}. \tag{15}$$

Considering that the simulation model of the sensor is accurate, covariance matrices $\mathbf{Q}$ and $\mathbf{R}$ were designed as

$$\mathbf{Q} = \begin{bmatrix} 10 & 0 & 0 \\ 0 & 0 & 0 \\ 0 & 0 & 0 \end{bmatrix} \quad \mathbf{R} = \begin{bmatrix} 0.0001 & 0 \\ 0 & 0.0025 \end{bmatrix}. \tag{16}$$

In the first simulation, we assumed that the MHD measurement signal was not over-range, and the amplitude (A) of Equation (14) was set to 0.2.

Figure 3a shows that the FOG measurements were inadequate for ensuring measurement accuracy in the middle- and high-frequency ranges, whereas the MHD sensor failed to capture low-frequency motion. Figure 3b presents the result obtained after Kalman filter fusion, with the fused output aligning well with the original velocity. Figure 3c compares the measurement and fusion errors, revealing that the latter remained nearly constant, while the measurement errors contained multiple frequency components. A statistical analysis of the fusion error was conducted, and Figure 3d demonstrates that the fusion result follows a normal distribution, effectively preserving the individual frequency components of the signal.

For comparison, the second simulation involved making the MHD measurements exceed the range. The amplitude A in Equation (14) was set to 2.

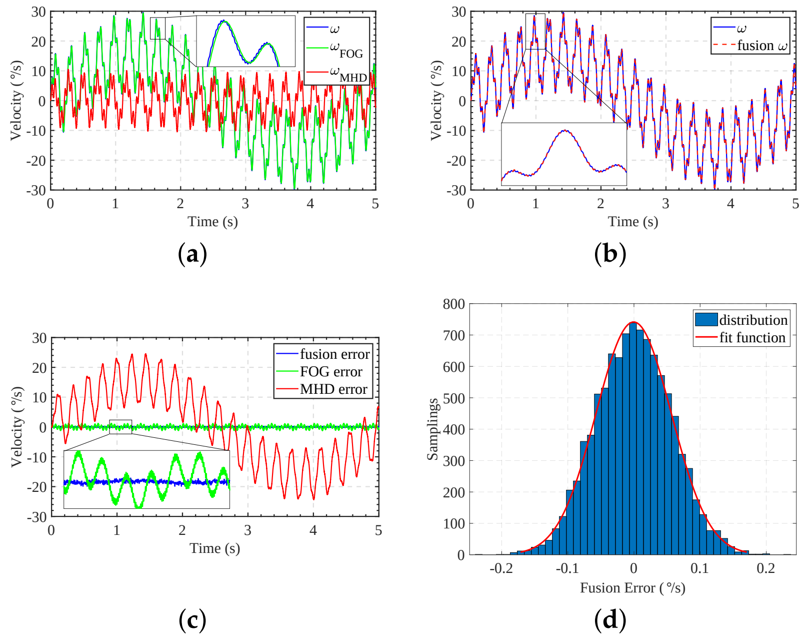

Figure 3. Simulation results for fusion of sensor measurements without over-range. (**a**) Original velocity and measurement results, (**b**) fusion results, (**c**) comparison of fusion error and measurement error, and (**d**) statistics of fusion error.

Figure 4a shows that the measurement range of the MHD sensor was limited to 0.5 rad/s, and when the signal exceeded this range, accurate measurements were no longer possible. Figure 4b,c present the results and errors, respectively, obtained after Kalman filter fusion, showing significant errors in the fused results due to the distortion caused by measurement saturation. Figure 4d demonstrates that the error included all frequency components of the signal, in contrast to the fusion results, where no over-range signal was produced, indicating that the fusion results were severely distorted.

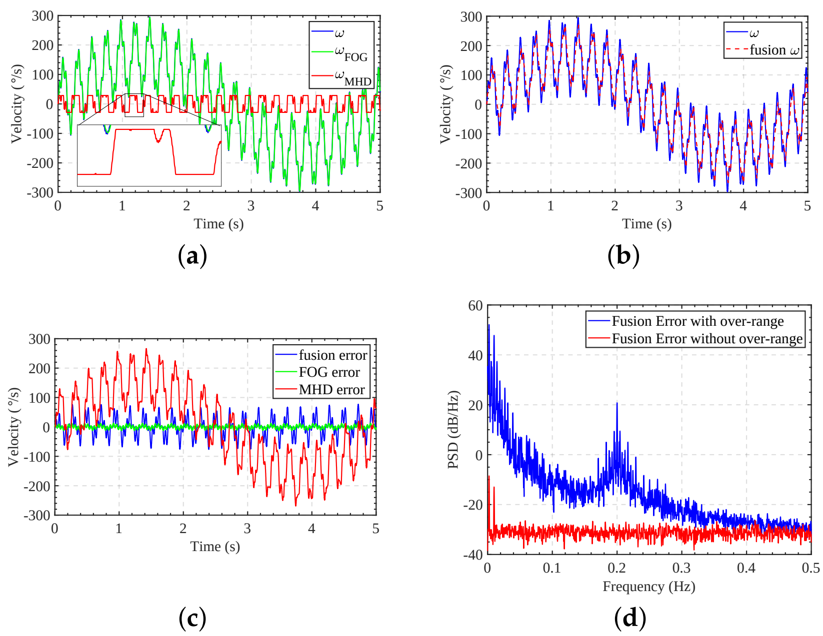

Figure 4. Simulation results for fusion of sensor measurements with over-range. (**a**) Original velocity and measurement results, (**b**) fusion results, (**c**) comparison of fusion error and measurement error, and (**d**) power spectrum of fusion errors.

4.2. Soft-Switching Adaptive Method Simulations

To verify the effectiveness of the SSAKF method when the MHD measurements exceeded the range, the amplitude in Equation (14) was set to 1, clearly distinguishing between over-range and non-over-range intervals. Compared with the fusion distortion results in Figure 4, Figure 5a,b show that, when measurements exceeded the range, with the proposed SSAKF method, the value of matrix $\bar{R}(k)$ was adaptively adjusted, reducing the weight of the MHD measurement in the fusion process and preventing overall distortion in the fusion results. On the other hand, when the measurements were within the range, the implementation of the SSAKF method effectively reduced fusion errors, ensuring that the error remained low.

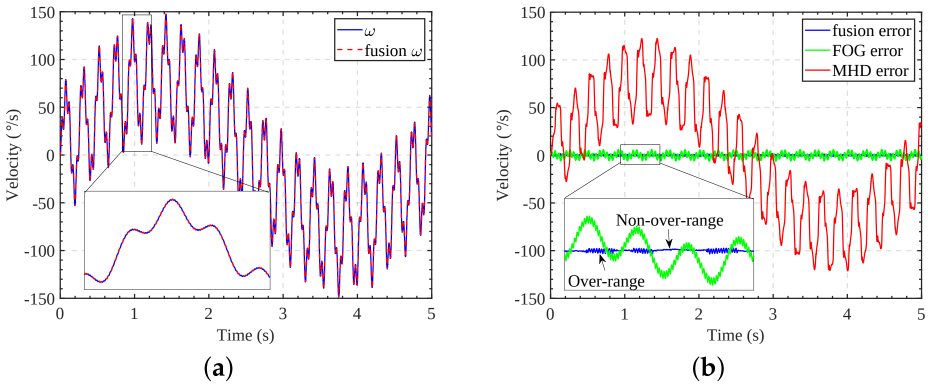

Figure 5. Simulation results for SSAKF of sensor measurements with over-range. (**a**) Fusion results and (**b**) comparison of fusion error and measurement error.

5. Experimental Validation

This section presents the frequency–domain models for both sensors. We then present the verification of the fusion algorithm based on a series of experiments, including static tests, composite–frequency assessments, random motion verification, and full-band sweeps. Throughout the experiments, the performance of the fusion algorithm is also compared with several traditional fusion methods.

5.1. Sensor System Identification

The Kalman filter requires obtaining the frequency–domain model of the sensor. Therefore, to acquire the transfer function for both sensors, we used a turntable with a bandwidth of 1000 Hz as the excitation source for the frequency sweep signal. This turntable does not belong to our team, so further experiments will not employ it on this platform.

The blue lines depicted in Figure 6a,b represent the identification results, while the fitting results of the frequency–domain curve are illustrated in green. The fitting results of the FOG model can be expressed as the following:

$$G_{FOG}(s) = \frac{200\pi(3000\pi)^2}{(s+200\pi)(s+6000\pi+(3000\pi)^2)}. \tag{17}$$

For the MHD model,

$$G_{MHD}(s) = \frac{25.5s(20000^2)}{(s+10.6\pi)(s+40000+(20000)^2)}. \tag{18}$$

Because of the intricate nature of the high-order model, adjusting the Kalman filter parameters is challenging. Consequently, by disregarding the high-frequency components arising from the backend amplification circuit, the low-order transfer function model, indicated by the red line, is approximated by

$$G_{FOG}(s) \approx \frac{200\pi}{s + 200\pi}, \quad G_{MHD}(s) \approx \frac{25.5s}{s + 10.6\pi}. \tag{19}$$

Equation (19) represents the corresponding transfer functions for the two sensors and serves as the basis for the simulations presented earlier. The state-space model of the Kalman filter is given by Equation (15).

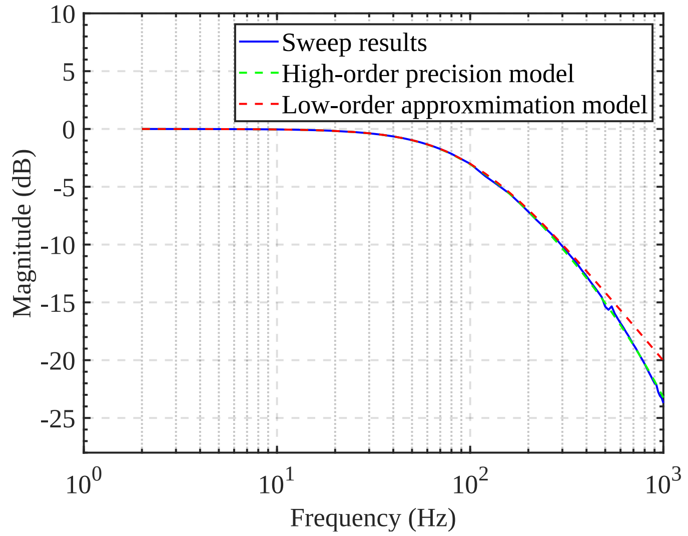

(**a**)

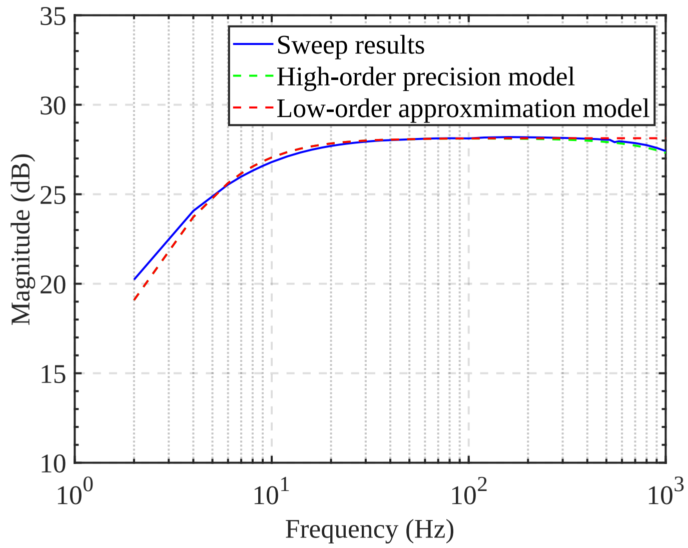

(**b**)

Figure 6. Frequency identification result. (**a**) FOG frequency response and (**b**) MHD frequency response.

5.2. Comparison Method

To verify the superiority and advancement of the proposed method, we used two traditional fusion schemes with different measurement frequency bands for experimental comparison.

5.2.1. Complementary Filtering Method [24]

The complementary filtering method is shown in Figure 7.

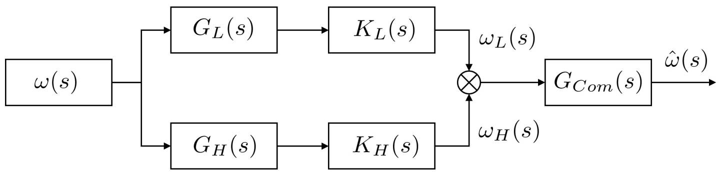

Figure 7. Complementary filtering method.

$G_L(s)$ and $G_H(s)$ are the transfer functions of the sensors. K_L and K_H are the scale factors. The complementary filter used to eliminate the amplitude bulge in the overlapping frequency band of the two sensors is designed as follows:

$$G_{Com}(s) = \frac{1}{G_L(s) + G_H(s)}. \tag{20}$$

However, the complementary filtering method necessitates a high degree of accuracy in the transfer function model. But owing to the model's significant complexity or high order, its physical achievement cannot be guaranteed. Consequently, a reduced-order approximation is required, which inevitably impacts the fusion outcome.

5.2.2. Closed-Loop Control Filtering [25]

Compared with the complementary filtering method, the closed-loop control filtering method does not require an accurate transfer function model (Figure 8). This method requires the design of a controller $G_c(s)$ to ensure that the closed-loop output tracks the low-frequency measurement results. The fusion output angular velocity $\hat{\omega}(s)$ can be expressed as

$$\hat{\omega}(s) = K_L G_{CL}(s) G_L(s)\omega(s) + K_H(1 - G_{CL}(s))G_H(s)\omega(s). \tag{21}$$

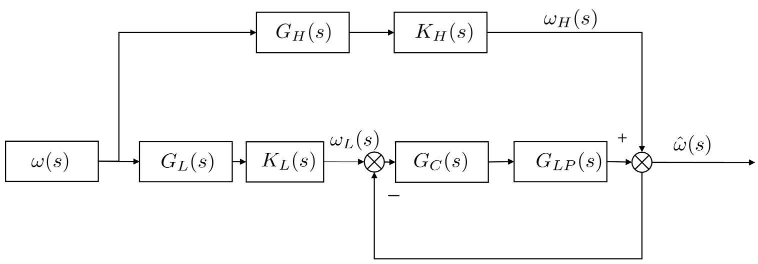

Figure 8. Closed-loop control filtering method.

By designing the transfer function $G_{CL}(s) = G_{LP}(s)G_C(s)/(1 + G_{LP}(s)G_C(s))$ to ensure that $G_{LP}(s) \approx 1$ in the low-frequency band and $G_{LP}(s) \approx 0$ in the high-frequency band, we can fuse the signal automatically.

This method also has flaws. Specifically, when the signal frequency falls within the range defined by the cutoff frequencies of the two sensors, the scale factor of the combined signal undergoes significant fluctuations. This happens because the transfer function must have a transition band, which cannot strictly guarantee that $G_{LP}(s) \approx 1$ in the low-frequency band and $G_{LP}(s) \approx 0$ in the high-frequency band.

5.3. Experimental Setup and Parameters

The experimental setup shown in Figure 9 consisted of a PC, a microprocessor STM32 board, a servo turntable, an MHD sensor, and a FOG. The turntable generates the required motion. The two sensors measured the angular velocity of the turntable. Moreover, the STM32 board was employed for turntable control, data acquisition, and fusion processing.

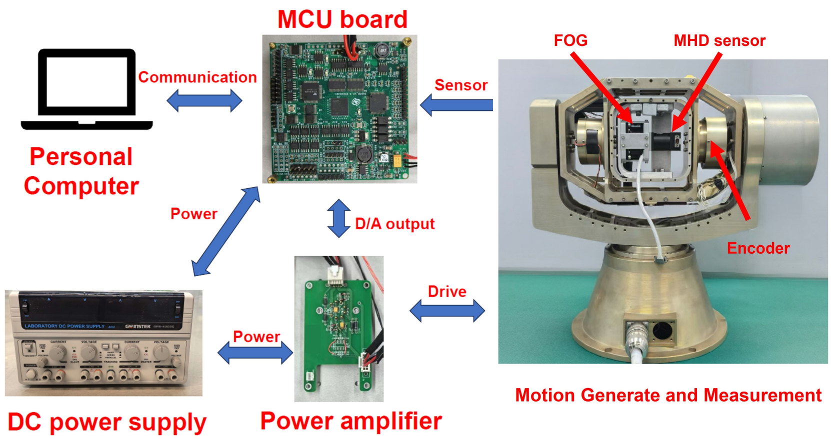

Figure 9. Experimental setup diagram.

Considering the discrepancies between the actual and nominal models, some parameters used in the experiments differed from those in the simulation. The specific parameter settings are shown in Table 3.

For the FOG measurements, the measurement range can reach up to more than 1000°/s, which is significantly higher than the upper limit of practical applications. Therefore, for $R(1,1)$, we do not employ the adaptive method, meaning $f(z_1(k))$ is always 1 and $f(z_2(k))$ uses the SSAKF method. This approach ensures that the FOG measurements are consistently considered in the estimation process, while the MHD measurements are adaptively adjusted based on the system's dynamic behavior.

Table 3. Parameter definitions of SSAKF.

Parameter	Value	Parameter	Value
$\mathbf{Q}$	$[10,0,0;\ 0,0,0;\ 0,0,0.008]$	Initial $\mathbf{P}$	$[1,1,1;\ 1,1,1;\ 1,1,1]$
$\mathbf{R}$	$[0.001,0;\ 0,0.01]$	α	0.6 s/°
β	249,999.5	τ	29 °/s

5.4. Experimental Results

The complete experiment consisted of four parts: static noise analysis, composite–frequency signals, random motion, and full-band sweeping. The results of each part are compared with those of the other two methods.

5.4.1. Static Fusion Test

In this part of the experiment, the data from the two sensors were measured statically. The static noise distribution was determined based on statistical analysis, and the power spectral density (PSD) of the noise was obtained.

Figure 10 shows the static noise PSD of different methods. The noise PSD of the SSAKF method transitioned smoothly from the low-frequency FOG noise level to the high-frequency MHD noise, remaining relatively flat. Moreover, the noise of the SSAKF method consistently remained between the MHD and the FOG, with its time–domain RMS being lower than that of other fusion methods. Because of model inaccuracies, the complementary filtering method exhibited higher noise power density at low frequencies compared with other methods, and the high-frequency also presented higher noise levels. The closed-loop combined filtering method produced peaks when transitioning to the high-frequency band, leading to an increase in the noise level. Table 4 also shows that the mean values of the methods were almost at the same level, while the RMS and mean values of the SSAKF were lower than those of the other two methods, indicating the superiority of this method under static conditions.

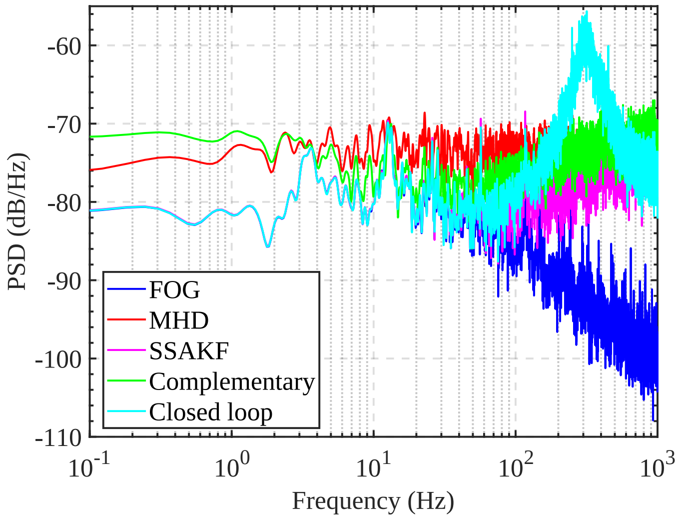

Figure 10. Static noise PSD analysis.

Table 4. Statistic information of static noise.

Methods	FOG	MHD	SSAKF	Complementary	Closed-Loop
Mean	-1.09×10^{-8}	2.72×10^{-7}	-4.60×10^{-8}	-9.81×10^{-8}	9.60×10^{-8}
RMS	0.0012	0.0072	0.0052	0.0132	0.0075

5.4.2. Composite-Frequency Assessments

In the composite–frequency part of the experiment, three signals were chosen to overlap and were located in the passband of the FOG (0–5 Hz), the passband of the MHD (100–1000 Hz), and the common passband (5–100 Hz).

The input function ($u(t)$) of the motor was designed as

$$u(t) = sin(5 \cdot 2\pi t) + sin(20 \cdot 2\pi t) + 5 \cdot sin(100 \cdot 2\pi t). \tag{22}$$

The experimental results are shown in Figure 11. The velocity signal revealed certain differences in the fusion results produced by different methods. However, these differences could not be effectively compared directly from the velocity signal. Therefore, the measurement and fusion results were integrated to obtain the corresponding angles, which were then compared with the encoder value.

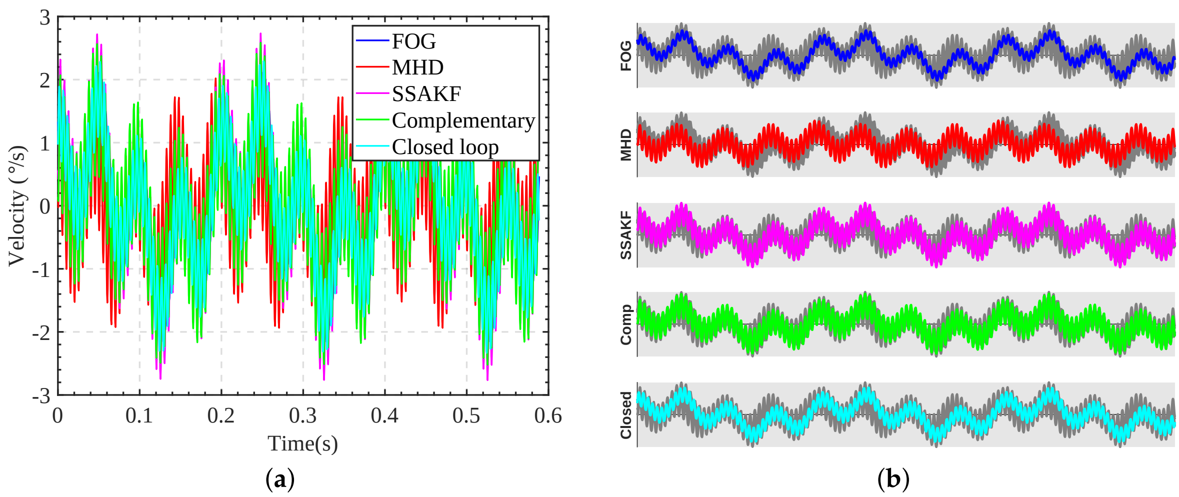

Figure 11. Composite–frequency signal fusion. (**a**) General view. (**b**) Details of each signal.

As shown in Figure 12, the pink line representing the integral of the Kalman filter fusion result closely follows the trend of the encoder measurement curve (comparison with the actual value limited by the encoder resolution), while the other two methods show varying degrees of error. The comparison verified that the SSAKF method provides a better measurement of the actual inertial angular velocity than the sensor alone and other fusion methods.

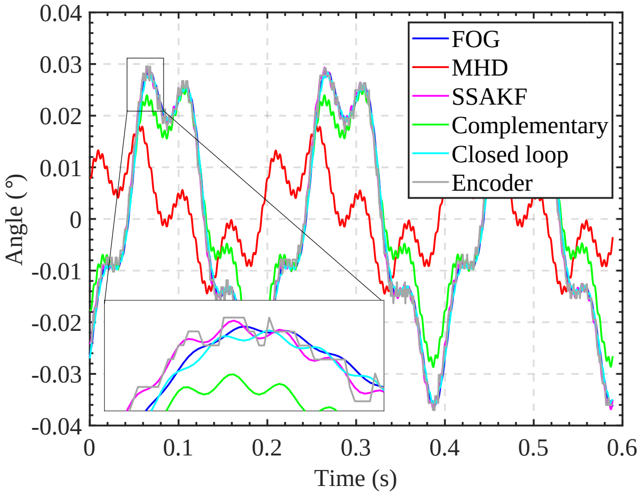

Figure 12. Integration of composite–frequency signal fusion.

5.4.3. Random Motion Verification

Unlike the previous two parts, in the random motion experiment, the structure remained mounted on the turntable, but instead of using a motor excitation source, we applied manual force to drive the shaft's motion, and its angular velocity was measured.

Figure 13a and Figure 13b present the velocity fusion results under two conditions: when the MHD sensor did not experience over-range and when its measurements exceeded the range. In the absence of over-range conditions, both the SSAKF and traditional Kalman filter methods were capable of providing accurate velocity estimates, and the fusion result showed consistency. However, when the MHD sensor measurements exceeded the range, the fusion result obtained by using the traditional Kalman filter exhibited significant errors, and the fused data even failed to be as accurate as with the FOG individual measurements. In contrast, the proposed SSAKF method effectively mitigated the influence of the MHD data during fusion, thereby producing a fused result that more closely approximated the true velocity.

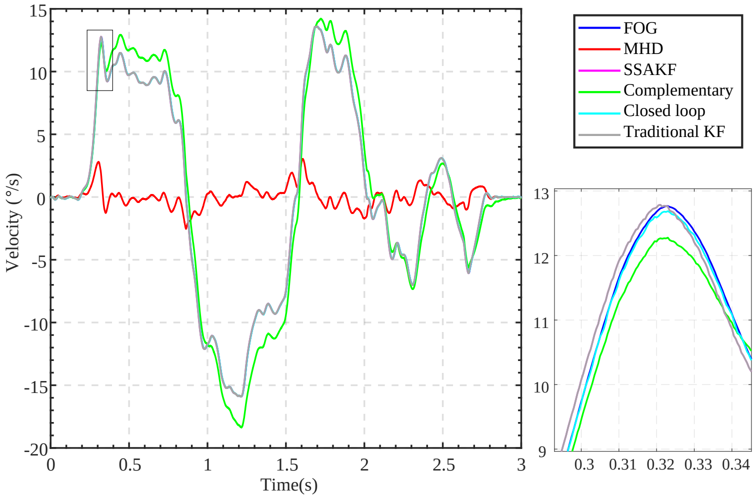

(**a**)

Figure 13. *Cont.*

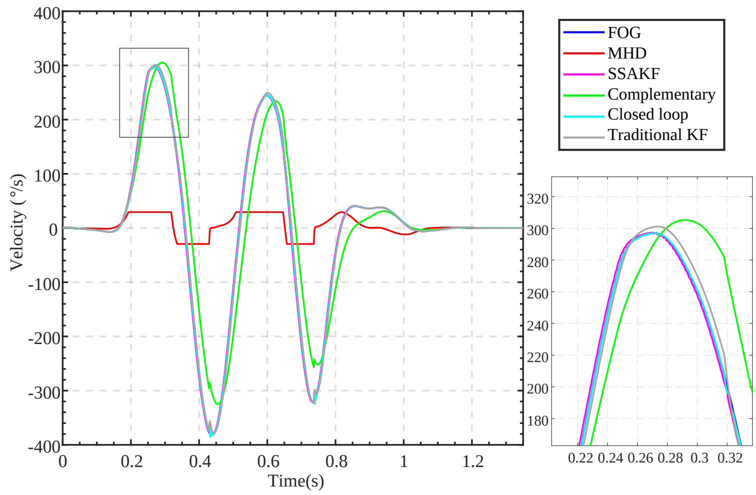

(**b**)

Figure 13. Random signal fusion. (**a**) Normal condition. (**b**) Over-range condition.

5.4.4. Full-Band SWEEP

In the sweep frequency experiment, a pseudo-random white noise signal was used as the motor excitation source. By comparing the time–domain fusion results of each sensor with the Bode diagram in the frequency domain, the frequency–domain relationship between various fusion methods and the two sensors was compared.

The time–domain experimental results with a pseudo-random noise excitation source passing through the motor are shown in Figure 14, and the frequency is shown in Figure 15.

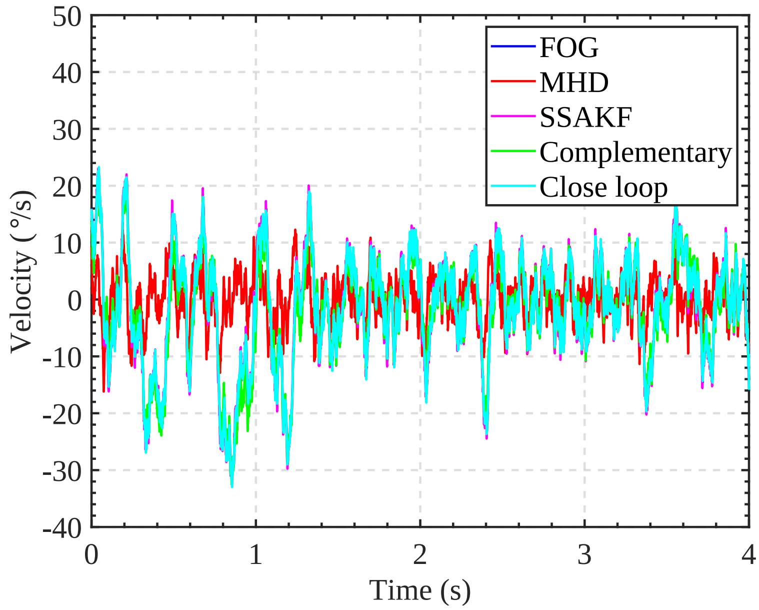

Figure 14. Time–domain response signal of noise sweep.

Of note, the sweep results indicate the angular velocity of the experimental platform, and the Bode diagrams are related to the mechanical structure, so the low-frequency collapse caused by friction and the high-frequency resonance and anti-resonance problems occurred.

By ignoring the influence of the mechanical structure and using the frequency–domain response results of the FOG and MHD as the benchmark, we see that the complementary filtering method had some errors in the frequency domain due to an inaccurate model.

Because of the existence of the transition band of the closed-loop filter, the closed-loop combined filtering method produced unexpected results in the middle band.

Compared with these two methods, the Kalman filter method demonstrated superior performance in extending the low-frequency bandwidth and maintaining accuracy. In the low-frequency band, the fusion result of the SSAKF overlapped with the low-frequency band of the FOG and with the measurement result of the MHD in the high-frequency band. The transition from low to high frequencies was smooth, with no resonance issues. Compared with the passbands of the two sensors, the amplitude fluctuation was less than 2 dB, and the phase fluctuation was less than 10°. This shows that the SSAKF method can effectively extend the low-frequency band of the MHD sensor and has high accuracy.

According to the analysis of the above experimental results, both the time- and frequency–domain outcomes demonstrate that the SSAKF method can be effectively used to obtain fusion measurement results under various operating conditions. Its implementation significantly extends the measurement bandwidth and allows one to obtain more accurate data for the closed-loop feedback of the platform.

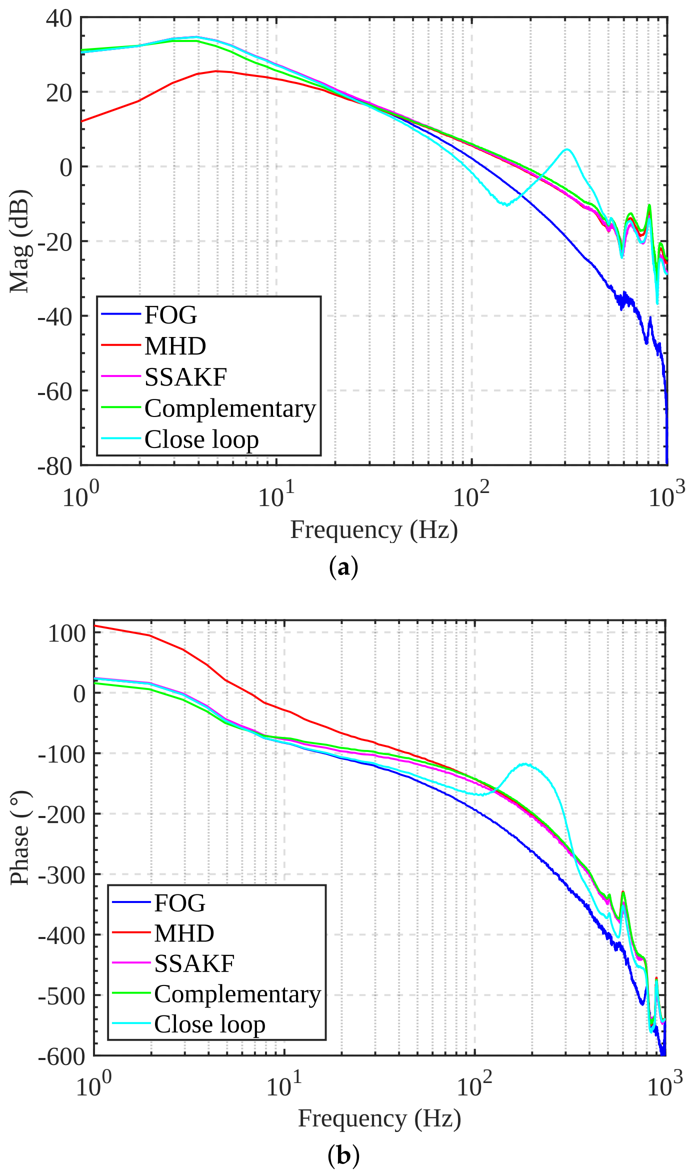

Figure 15. Frequency–domain Bode plots. (**a**) Magnitude response. (**b**) Phase response.

6. Conclusions

This study developed a Kalman filter with a novel soft-switching adaptive law for signal fusion. The fusion method can be used to effectively combine and measure two signals with different frequency bands, ensuring the correctness of the fusion result even when one signal exceeds its measurement range. The proposed method was validated through a series of experiments, demonstrating its effectiveness and advanced capabilities. However, to simplify parameter adjustment, the model was simplified to some extent. For the model uncertainties caused by simplification and non-ideal characteristics, we will further quantify the relationship between these uncertainty and the **Q** matrix. This will enable more precise tuning of the **Q** matrix, ultimately improving fusion performance and reducing errors.

Author Contributions: Conceptualization, J.T.; methodology, J.T. and S.S.; software, J.T. and F.W.; validation, J.T. and S.S.; formal analysis, J.T.; investigation, S.S. and J.T.; resources, D.T. and F.W.; writing—original draft preparation, J.T. and S.S.; writing—review and editing, D.T. and F.W.; visualization, J.T.; supervision, D.T.; project administration, D.T.; funding acquisition, D.T. All authors have read and agreed to the published version of the manuscript.

Funding: This research was funded by the National Key R&D Plan 2022YFF1302000, in part by CAS Project for Young Scientists in Basic Research YSBR-066, in part by the National Science Foundation of China under Grant 62475260 and 12203049 and the Youth Innovation Promotion Association of the Chinese Academy of Sciences 2023230.

Data Availability Statement: Publicly available datasets were analyzed in this study. This data can be found here: https://github.com/sky9785/SSAKF_data.git.

Conflicts of Interest: The authors declare no conflicts of interest.

Abbreviations

The following abbreviations are used in this manuscript:

MHD	Magneto-hydrodynamics
SSAKF	Soft-switch Adaptive Kalman Filter
FOG	Fiber-optic gyro
PSD	Power spectral density
RMS	Root-Mean-Square
EMF	Electromotive force
MEMS	Micro-Electro-Mechanical Systems

Appendix A. Derivation of Linear Combination Rewriting of Kalman Filter

According to the matrix inversion lemma

$$(\mathbf{A}+\mathbf{BCD})^{-1}=\mathbf{A}^{-1}-\mathbf{A}^{-1}\mathbf{B}(\mathbf{DA}^{-1}\mathbf{B}+\mathbf{C}^{-1})^{-1}\mathbf{DA}^{-1}, \tag{A1}$$

the a-posteriori estimate covariance $\mathbf{P}(k)$ can be rewritten as

$$\mathbf{P}(k)=[(\mathbf{P}^{-}(k))^{-1}+\mathbf{H}^{T}\mathbf{R}^{-1}\mathbf{H}]^{-1}, \tag{A2}$$

so rewriting the Kalman gain $\mathbf{K}(k)$ equation, we can get

$$\mathbf{K}(k)=\mathbf{P}^{-}(k)\mathbf{H}^{T}[\mathbf{R}^{-1}-\mathbf{R}^{-1}\mathbf{HP}(k)\mathbf{H}^{T}\mathbf{R}^{-1}]. \tag{A3}$$

Now, by modifying Equation (A3) and substituting Equation (A2) into it, we obtain the following result:

$$\begin{aligned}\mathbf{K}(k)\mathbf{R}(\mathbf{H}^T)^{-1} &= \mathbf{P}^-(k) - \mathbf{P}^-(k)\mathbf{H}^T\mathbf{R}^{-1}\mathbf{H}\mathbf{P}(k) \\ &= \mathbf{P}^-(k) - \mathbf{P}^-(k)[\mathbf{H}^T\mathbf{R}^{-1}\mathbf{H}\mathbf{P}^-(k)^{-1} + \mathbf{P}^-(k)^{-1}]\mathbf{P}(k) + \mathbf{P}(k) \\ &= \mathbf{P}(k),\end{aligned} \tag{A4}$$

which also means

$$\mathbf{K}(k) = \mathbf{P}(k)\mathbf{H}^T\mathbf{R}^{-1}. \tag{A5}$$

Finally, according to Equations (A5) and (5), the estimate state $\hat{\mathbf{x}}(k)$ can be re-expressed as a linear combination:

$$\begin{aligned}\hat{\mathbf{x}}(k) &= \hat{\mathbf{x}}^-(k) + \mathbf{K}(k)[\mathbf{z}(k) - \mathbf{H}\hat{\mathbf{x}}^-(k)] \\ &= [\mathbf{I} - \mathbf{K}(k)\mathbf{H}]\hat{\mathbf{x}}^-(k) + \mathbf{K}(k)\mathbf{z}(k) \\ &= \mathbf{P}(k)[\mathbf{P}^-(k)]^{-1}\hat{\mathbf{x}}^-(k) + \mathbf{P}(k)\mathbf{H}^T\mathbf{R}^{-1}\mathbf{z}(k) \\ &= \mathbf{C}_p(k)\hat{\mathbf{x}}^-(k) + \mathbf{C}_m(k)\mathbf{z}(k),\end{aligned} \tag{A6}$$

where

$$\begin{aligned}\mathbf{C}_p(k) &= \mathbf{P}(k)[\mathbf{P}^-(k)]^{-1} \\ \mathbf{C}_m(k) &= \mathbf{P}(k)\mathbf{H}^T\mathbf{R}^{-1}.\end{aligned} \tag{A7}$$

References

1. Ren, W.; Wang, Z.; Xia, M.; Lin, H. MFINet: Multi-Scale Feature Interaction Network for Change Detection of High-Resolution Remote Sensing Images. *Remote Sens.* **2024**, *16*, 1269. [CrossRef]
2. Xiang, S.; Liang, Q. Remote sensing image compression based on high-frequency and low-frequency components. *IEEE Trans. Geosci. Remote Sens.* **2024**, *62*, 1–15. [CrossRef]
3. Jia, P.; Chen, C.; Zhang, D.; Sang, Y.; Zhang, L. Semantic segmentation of deep learning remote sensing images based on band combination principle: Application in urban planning and land use. *Comput. Commun.* **2024**, *217*, 97–106. [CrossRef]
4. Ran, T.; Shi, G.; Lin, J.; Meng, L. Decoupling Control of an Aviation Remote Sensing Stabilization Platform Based on a Cerebellar Model Articulation Controller. *Machines* **2023**, *11*, 5. [CrossRef]
5. Ge, Q.; Li, Y.; Wang, Y.; Hu, X.; Li, H.; Sun, C. Adaptive Kalman Filtering Based on Model Parameter Ratios. *IEEE Trans. Autom. Control* **2024**, *69*, 6230–6237. [CrossRef]
6. Dahlin Rodin, C.; de Alcantara Andrade, F.A.; Hovenburg, A.R.; Johansen, T.A. A Survey of Practical Design Considerations of Optical Imaging Stabilization Systems for Small Unmanned Aerial Systems. *Sensors* **2019**, *19*, 4800. [CrossRef]
7. Hilkert, J. Inertially stabilized platform technology concepts and principles. *IEEE Control Syst. Mag.* **2008**, *28*, 26–46.
8. Jain, A.; Kanhangad, V. Human activity classification in smartphones using accelerometer and gyroscope sensors. *IEEE Sens. J.* **2017**, *18*, 1169–1177. [CrossRef]
9. Xu, M.; Mo, J.; Xia, C.; Yang, L.; Ji, F.; Chen, J.; Li, X. Error analysis and modeling of the racetrack magnetohydrodynamic linear motion sensor. *Meas. Sci. Technol.* **2024**, *35*, 046118. [CrossRef]
10. Tuo, W.; Li, X.; Ji, Y.; Wu, T.; Xia, G. Quantitative analysis of position setting effect on magnetohydrodynamics angular vibration sensor response. *Sensors Actuators A Phys.* **2021**, *332*, 113194. [CrossRef]
11. Capriglione, D.; Carratù, M.; Catelani, M.; Ciani, L.; Patrizi, G.; Pietrosanto, A.; Sommella, P. Experimental analysis of filtering algorithms for IMU-based applications under vibrations. *IEEE Trans. Instrum. Meas.* **2020**, *70*, 1–10. [CrossRef]
12. Mehamud, I.; Marklund, P.; Björling, M.; Shi, Y. Machine condition monitoring enabled by broad range vibration frequency detecting triboelectric nano-generator (TENG)-based vibration sensors. *Nano Energy* **2022**, *98*, 107292. [CrossRef]
13. Łakomy, K.; Madonski, R.; Dai, B.; Yang, J.; Kicki, P.; Ansari, M.; Li, S. Active disturbance rejection control design with suppression of sensor noise effects in application to DC–DC buck power converter. *IEEE Trans. Ind. Electron.* **2021**, *69*, 816–824.
14. Kong, L.; Peng, X.; Chen, Y.; Wang, P.; Xu, M. Multi-sensor measurement and data fusion technology for manufacturing process monitoring: A literature review. *Int. J. Extrem. Manuf.* **2020**, *2*, 022001. [CrossRef]
15. Xiang, C.; Feng, C.; Xie, X.; Shi, B.; Lu, H.; Lv, Y.; Yang, M.; Niu, Z. Multi-sensor fusion and cooperative perception for autonomous driving: A review. *IEEE Intell. Transp. Syst. Mag.* **2023**, *15*, 36–58. [CrossRef]

16. Liu, W.; Liu, Y.; Bucknall, R. Filtering based multi-sensor data fusion algorithm for a reliable unmanned surface vehicle navigation. *J. Mar. Eng. Technol.* **2023**, *22*, 67–83. [CrossRef]
17. Ding, X.; Wang, Z.; Zhang, L.; Wang, C. Longitudinal vehicle speed estimation for four-wheel-independently-actuated electric vehicles based on multi-sensor fusion. *IEEE Trans. Veh. Technol.* **2020**, *69*, 12797–12806. [CrossRef]
18. Zhang, Q.; Tan, Z.; Guo, L. A New Controller of Stabilizing Circuit in FOGS. In Proceedings of the 2009 IEEE International Conference on Mechatronics and Automation, Changchun, China, 9–12 August 2009; Conference Proceedings; Guo, S., Fukuda, T., Yo, Y., Yu, H., Eds.; IEEE: Piscataway, NJ, USA, 2009; Volumes 1–7. pp. 757–761.
19. Dickson, W.C.; Yee, T.K.; Coward, J.F.; McClaren, A.; Pechner, D.A. Compact fiber optic gyroscopes for platform stabilization. In Proceedings of the Nanophotonics and Macrophotonics for Space Environments VII, San Diego, CA, USA, 25–27 August 2013; Taylor, E., Cardimona, D., Eds.; SPIE: Bellingham, WA, USA, 2013; Volume 8876. [CrossRef]
20. Sofla, M.S.; Zareinejad, M.; Parsa, M.; Sheibani, H. Integral based sliding mode stabilizing a camera platform using Kalman filter attitude estimation. *Mechatronics* **2017**, *44*, 42–51. [CrossRef]
21. Koenigseder, F.; Kemmetmueller, W.; Kugi, A. Attitude Estimation Using Redundant Inertial Measurement Units for the Control of a Camera Stabilization Platform. *IEEE Trans. Control Syst. Technol.* **2016**, *24*, 1837–1844. [CrossRef]
22. Tian, Y.; Compere, M.; Drakunov, S. A Quaternion-Based Sliding Mode Observer for Gyro-Bias Estimation and Attitude Reconstruction. In Proceedings of the Proceedings of the Asme International Mechanical Engineering Congress and Exposition, Salt Lake City, UT, USA, 8–14 November 2019; ASME: New York, NY, USA, 2020; Volume 4.
23. Lu, P.; Dai, F. An overview of multi-sensor information fusion. In Proceedings of the 2021 6th International Conference on Intelligent Informatics and Biomedical Sciences (ICIIBMS), Oita, Japan, 25–27 November 2021; IEEE: Piscataway, NJ, USA, 2021; Volume 6, pp. 5–9.
24. Rehman, S.; Khan, M.F.; Kim, H.D.; Kim, S. Energy-efficient and reconfigurable complementary filter based on analog-digital hybrid computing with SnS_2 memtransistor. *Nano Energy* **2023**, *109*, 108333. [CrossRef]
25. Möller, F.; Essig, T.; Holzhauer, S.; Förstner, R. Experimental demonstration of a method to actively stabilize satellite structures against random perturbations of thermal boundary conditions using a closed-loop filter and controller approach. *CEAS Space J.* **2024**, *16*, 427–444. [CrossRef]
26. Rizun, P. Optimal Wiener filter for a body mounted inertial attitude sensor. *J. Navig.* **2008**, *61*, 455–472. [CrossRef]
27. Kheirandish, M.; Yazdi, E.A.; Mohammadi, H.; Mohammadi, M. A fault-tolerant sensor fusion in mobile robots using multiple model Kalman filters. *Robot. Auton. Syst.* **2023**, *161*, 104343. [CrossRef]
28. Alfian, R.I.; Ma'arif, A.; Sunardi, S. Noise reduction in the accelerometer and gyroscope sensor with the Kalman filter algorithm. *J. Robot. Control (JRC)* **2021**, *2*, 180–189. [CrossRef]
29. Potokar, E.R.; Norman, K.; Mangelson, J.G. Invariant extended kalman filtering for underwater navigation. *IEEE Robot. Autom. Lett.* **2021**, *6*, 5792–5799. [CrossRef]
30. Lu, L.; Ding, W.; Xiong, F.; Liang, T.; Fu, R.; Zhang, N. Attitude Estimation Algorithm of Unmanned Aerial Vehicle Based on Untraced Kalman Filter. In Proceedings of the 2023 4th International Seminar on Artificial Intelligence, Networking and Information Technology (AINIT), Nanjing, China, 16–18 June 2023; IEEE: Piscataway, NJ, USA, 2023; pp. 560–563.
31. Xu, W.; Huang, C.; Jiang, H. Analyses and enhancement of linear Kalman-filter-based phase-locked loop. *IEEE Trans. Instrum. Meas.* **2021**, *70*, 6504510. [CrossRef]
32. Xiong, K.; Wei, C.; Zhang, H. Q-learning for noise covariance adaptation in extended KALMAN filter. *Asian J. Control* **2021**, *23*, 1803–1816. [CrossRef]
33. Song, M.; Astroza, R.; Ebrahimian, H.; Moaveni, B.; Papadimitriou, C. Adaptive Kalman filters for nonlinear finite element model updating. *Mech. Syst. Signal Process.* **2020**, *143*, 106837. [CrossRef]
34. Gajula, K.; Marepalli, L.K.; Yao, X.; Herrera, L. Recursive least squares and adaptive Kalman filter-based state and parameter estimation for series arc fault detection on DC microgrids. *IEEE J. Emerg. Sel. Top. Power Electron.* **2021**, *10*, 4715–4724. [CrossRef]
35. Mumuni, F.; Mumuni, A. Adaptive Kalman filter for MEMS IMU data fusion using enhanced covariance scaling. *Control Theory Technol.* **2021**, *19*, 365–374. [CrossRef]
36. Zhu, M.; Wu, Q.; Wang, Y. Forecasting gas consumption based on a residual auto-regression model and kalman filtering algorithm. *J. Resour. Ecol.* **2019**, *10*, 546–552.
37. Lee, A.S.; Hilal, W.; Gadsden, S.A.; Al-Shabi, M. Combined Kalman and sliding innovation filtering: An adaptive estimation strategy. *Measurement* **2023**, *218*, 113228. [CrossRef]
38. Kumari, N.; Kulkarni, R.; Ahmed, M.R.; Kumar, N. Use of kalman filter and its variants in state estimation: A review. *Artif. Intell. Sustain. Ind.* **2021**, *4*, 213–230.
39. Ji, Y.; Li, X.; Wu, T.; Chen, C. Modified analytical model of magnetohydrodynamics angular rate sensor for low-frequency compensation. *Sens. Rev.* **2016**, *36*, 193–199. [CrossRef]

40. Ji, Y.; Xu, M.; Li, X.; Wu, T.; Tuo, W.; Wu, J.; Dong, J. Error Analysis of Magnetohydrodynamic Angular Rate Sensor Combing with Coriolis Effect at Low Frequency. *Sensors* **2018**, *18*, 1921. [CrossRef]
41. Laughlin, D.; Sebesta, H.; Eckelkamp-Baker, D. A dual function magnetohydrodynamic(MHD) device for angular motion measurement and control. *Adv. Astronaut. Sci.* **2002**, *111*, 335–347.